Soft Matter

The effect of alignment on the rate-dependent behavior of a main-chain liquid crystal elastomers

Journal:	*Soft Matter*
Manuscript ID	SM-ART-01-2020-000125.R2
Article Type:	Paper
Date Submitted by the Author:	18-Jul-2020
Complete List of Authors:	Martin Linares, Cristina Pilar; Johns Hopkins University, Mechanical Engineering Traugutt, Nicholas; University of Colorado at Denver , Mechanical Engineering Saed, Mohand; University of Cambridge, Cavendish Laboratory Martin Linares, Alejandro; Johns Hopkins University, Mechanical Engineering Yakacki, Christopher; University of Colorado Denver, Mechanical Engineering Nguyen, Thao; Johns Hopkins University,

The effect of alignment on the rate-dependent behavior of a main-chain liquid crystal elastomers

Cristina P. Martin Linares[a], Nicholas A. Traugutt[b], Mohand Saed[c], Alejandro Martin Linares[a], Christopher M. Yakacki[b], Thao D. Nguyen[a,*]

[a]*Department of Mechanical Engineering, The Johns Hopkins University, Baltimore, MD, USA*
[b]*Department of Mechanical Engineering, University of Colorado Denver, Denver, CO, USA*
[c]*Department of Physics, University of Cambridge, Cambridge, UK*

Abstract

This study investigated the effect of alignment on the rate-dependent behavior of a main-chain liquid crystal elastomer (LCE). Polydomain nematic LCE networks were synthesized from a thiol-acrylate Michael addition reaction in the isotropic state. The polydomain networks were stretched to different strain levels to induce alignment then crosslinked in a second stage photopolymerization process. The LCE networks were subjected to dynamic mechanical tests to measure the temperature-dependent storage modulus and uniaxial tension load-unload tests to measure the rate-dependence of the Young's modulus, mechanical dissipation, and characteristics of the soft stress response. Three-dimensional (3D) digital image correlation (DIC) was used to characterize the effect of domain/mesogen relaxation on the strain fields. All LCE networks exhibited a highly rate-dependent stress response with significant inelastic strains after unloading. The Young's modulus of the loading curve and hysteresis of the load-unload curves showed a power-law dependence on the strain rate. The Young's modulus increased with alignment and larger anisotropy and a smaller power-law exponent was measured for the Young's modulus and hysteresis for the highly aligned monodomains. The polydomain and pre-stretched networks loaded perpendicular to the alignment direction exhibited a soft stress response that featured a rate-dependent peak stress, strain-softening, and strain-stiffening. The 3D-DIC strain fields for the polydomain network and programmed networks stretched in the perpendicular direction were highly heterogeneous, showing regions of alternating higher and lower strains. The strain variations increased initially with loading, peaked during the strain softening part of the stress response, then decreased during the strain stiffening part of the stress response. Greater variability was measured for lower strain rates. These observations suggest that local domain/mesogen relaxation led to the development of the heterogeneous strain patterns and strain softening in stress response. These findings improved understanding of the kinetics of mesogen relaxation and its contributions to the rate-dependent stress response and mechanical dissipation.

Keywords: Liquid crystal elastomers, networks relaxation, Mesogen relaxation, 3D Digital Image Correlation, Soft elasticity, Viscoelasticity, Polydomain, Monodomain

1. Introduction

Liquid crystal elastomers (LCEs) are composed of stiff, anisotropically shaped molecular components, called mesogens, bound in a flexible network. The mesogens can self-organize under thermodynamically favorable conditions to create long-range order. Thermotropic LCEs with rod-shaped mesogens exhibit nematic ordering, where the mesogens align along a dominant orientation, called a director, below the isotropic-nematic transition temperature (T_{ni}). The ability of mesogens to rotate relative to the networks chains gives rise to many unique behaviors [1], including stress-optical effects [2, 3], axial actuation through the nematic-isotropic transition [4, 5], a soft stress response under quasistatic and dynamic loading [4, 6, 7], and enhanced dissipation that manifests over a wide range of

*Corresponding author
Email address: vicky.nguyen@jhu.edu (Thao D. Nguyen)

temperatures, frequencies, and loading rates [8, 9, 10]. These phenomena are more dramatic when the mesogens are incorporated into the backbone of the polymer chain, in a main-chain configuration, rather than on branches of the polymer chains, in a side-chain configuration. The direct coupling of main-chain LCEs, compared to the side-chain configurations, provides the highest chain anisotropy and allows more mesogen rotation and chain deformation than other configuration [11].

LCEs in the nematic state can exhibit a monodomain or polydomain microstructure depending on whether the mesogens were aligned during networks synthesis. Monodomains are characterized by a single global director, while polydomains are composed of micrometer-sized domains with local nematic ordering. The domains are oriented randomly giving polydomains a macroscopically isotropic behavior. Stretching a polydomain causes both the networks chains to deform and the domains to rotate towards the loading direction to form a monodomain [6, 12, 13]. This process turns the opaque polydomain transparent and produces a semi-soft stress response, characterized by a linear region, a peak stress upon initiation of domain rotation, strain-softening, and strain-stiffening [4, 14, 15, 16, 13, 9]. The strain softening region may appear as a flat plateau for some range of temperatures and strain rates, depending on the domain structure, and the equilibrium stress response of polydomains formed in the nematic state continually increases after the peak stress [15, 16, 9]. Exposing the programmed networks to a secondary crosslinking process fixes the monodomain structure, with the degree of chain alignment and mesogen order determined by the applied stretch.

Azoug *et al.* [9] showed that the semi-soft stress response of an acrylate main-chain polydomain LCE is highly dependent on the strain rate and temperature. Time-temperature superposition was used to characterize the rate-dependent stress response over a wide range of strain rates from 10^{-8}/s - 1/s. The Young's modulus, peak stress, and begin and end strain of the soft stress region at room temperature varied significantly with strain rates greater than 10^{-3}/s. Unloading at the same strain rate resulted in large inelastic strains and hysteresis. The inelastic strain was fully recovered after 2-15 minutes, indicating that stress response remained viscoelastic throughout the polydomain-monodomain transition. The mechanical dissipation under large deformation cyclic loading was investigated further for the same main-chain polydomain [10]. Previous experimental studies of side-chain polydomains also reported a rate-dependent soft stress response with similar features [15, 6]. The soft stress region extended over a narrower strain range for the side-chain LCEs, and rate-dependence was observed for lower strain rates, below 10^{-3}/s. For a siloxane side-chain polydomain, Clarke *et al.* [6] showed that the end of the equilibrium soft stress region was determined by the chain anisotropy, and the stress response after the polydomain-monodomain transition for all strain rates (10^{-7}/s-10^{-3}/s) collapsed back onto the equilibrium curve. Molecular dynamics simulations also showed that the stress response at different strain rates merged back to the equilibrium curve after the soft region [13]. These findings suggest that domain rotation is the dominant viscoelastic mechanism of the polydomain-monodomain transition and the stress response became rate-independent after domain alignment.

The relaxation mechanisms of various side-chain LCEs have also been studied by measuring the stress relaxation [14, 17, 15] and strain recovery response [18, 9]. Hotta and Terentjev [15] fit two power-laws to the master curve of the relaxation function of an acrylate side-chain polydomain, and found that the 0.15 exponent of the slower power-law was similar to that for classical rubbers. They attributed the faster 0.67 power-law exponent to domain rotation. Urayama and coworkers [19, 18] measured the strain recovery response of swollen acrylate monodomain and polydomains deformed by an electric field. The momodomains were aligned by surface anchoring before crosslinking. The authors remarked that strain recovery occurred within 1 s for monodomains, but required 10^3 s for polydomains [18], and attributed the slower recovery time to the disordered distribution of domains. These findings suggest that the degree of mesogen/domain alignment can significantly affect the rate-dependent stress response and mechanical dissipation of LCEs. While studies have compared the small strain dynamic viscoelastic response of monodomain and polydomain networks [20, 21] and of monodomain loaded in various orientations relative to the director orientation [22, 23], the effects of mesogen and domain reorientation on the large strain, rate-dependent stress response and dissipation remain poorly understood.

The purpose of this study was to systematically investigate the effect of alignment on the rate-dependent anisotropic stress response of an acrylate main-chain LCE. Programmed networks were synthesized from a two-stage thiol-acrylate Michael addition reaction that produced polydomain LCEs in the first stage. The networks were stretched to different strain levels corresponding approximately to the beginning and end of the polydomain-monodomain transition and the excess acrylate groups were crosslinked by photopolymerization in the second stage reaction. Polydomain

networks were also photopolymerized without stretching. The polydomain and pre-stretched networks were subjected to dynamic mechanical tests and load-unload tests, parallel and perpendicular to the director, and at different strain rates to compare the effect of alignment and director orientation on the rate dependence of the modulus, soft stress region, and dissipation. We also applied 3D-DIC to measure the evolving strain field during loading and unloading at different strain rates to characterize the dynamics of domain and mesogen relaxation and the effects on the strain field and stress response. Previously, two-dimensional (2D) DIC was applied to characterize the time-dependent evolution of the Poisson's ratio for polydomain and cholesteric LCE by Pritchard et al. [24] and the inhomogeneous soft elastic behavior of LCEs with locally patterned molecular orientation by Ware et al. [25].

2. Methods

2.1. Materials

Pentaerythritol tetra(3-mercaptopropionate) (PETMP), 1,3-propanedithiol (C3), phenylbis(2,4,6-trimethylbenzoyl) phosphine oxide (PPO), 2,6-di-tert-butylphenol (BHT), triethylamine (TEA), and toluene were purchased from Sigma Aldrich (St. Louis, MO, USA). 1,4-Bis-[4-(3-acryloyloxypropyloxy) benzoyloxy]-2-methylbenzene (RM257) was purchased from Wilshire Technologies (Princeton, NJ, USA). All of the materials were used as-received without purification. Main-chain LCEs were synthesized using a nonstoichiometric, two-stage thiol-acrylate Michael addition reaction developed by the Yakacki research group [26, 27]. The study by Saed et al. [28] showed that purification of materials should be unnecessary as the thiol-acrylate conversion is seen to be near complete (100%) within a short timeframe (5 hours at 22°C). To prepare the samples, first the acrylated-mesogen (RM 257) was added to a vial with 2 wt% inhibitor (BHT) and 30 wt% organic solvent (toluene). The vial was then heated to 100°C until the mesogens dissolved into a clear liquid solution. Next, difunctional thiol spacer (C3) and tetrafunctional thiol crosslinker (PETMP) were added at a ratio of 9:1 mol%, respectively. The two thiol monomers were added to the mesogen solution such that a 1.02:1 mol% ratio of acrylated-mesogen to thiols was achieved. In other words, there would be a 2 mol% excess of acrylate end groups to thiol groups to allow for a second stage photo-crosslinking reaction. Additionally, 2 wt% photoinitiator (PPO) was added to the solution, mixed using a vortex mixer for 30 seconds, and was heated at 100°C until the solution was clear again. The vial was immediately removed from the oven and 0.3 wt% addition reaction catalyst (TEA) was added. The solution was mixed for 30 seconds using a vortex mixer and air bubbles were removed in a vacuum chamber at 500 mm Hg for 30 seconds. The solution was then removed from vacuum and immediately poured into prepared molds made from 4.5 in. $\times$ 5.25 in. glass slides clamped together with binder clips around a 2 mm thick 3D printed PLA slide spacer and left to cure for 24 hours at room temperature. Once polymerized, samples were removed from their molds and left in a heated vacuum chamber at 100°C and 500 mmHg for 12 hours to remove the toluene from the LCE samples. Initial studies showed that specimens thinner than 2 mm were too compliant for accurate force measurements at low strains in uniaxial tension tests for accurate determination of the rate-dependent Youngs modulus and peak stress of the soft stress response. Thinner specimens were also too compliant for the DMA to properly compensate for the force needed to maintain the sinusoidal strains on the sample. Initial DMA testing on thinner samples produced sporadic noise that could not be filtered or smoothed for temperatures $T_{ni} \pm 30$°C, making it impossible to characterize the storage modulus and tanδ responses within these temperature ranges.

In the second stage, the LCE sheets were stretched uniaxially by 30% and 90% between 2 clamps in a custom fixture and held for 2 minutes to equilibrate the chain deformation and mesogen reorientation. The stretch was measured from the displacements of 2 dots drawn in the center of the sheet with each dot approximately 7 mm from the clamps. In prior testing, a 30% strain corresponded to the beginning of the soft stress region, where the domains began to reorient towards the loading direction but remained largely disorganized, while 90% strain was near the end of the soft stress region [9]. The networks became transparent upon stretching to 90%, which indicated that the domains/mesogens were highly aligned and formed a monodomain. Previous works have also used 90% strain to program a monodomain structure for a thiol-acrylate main-chain LCE [21]. The pre-stretched networks were exposed to UV light (365 nm) on both sides for 120 minutes each to photo-polymerize the excess acrylate groups at room temperature. The polydomain networks were not stretched before the second stage UV crosslinking. The sheets were released from the clamp, thermally cycled by a heating to 130°C and then cooled to room temperature to verify the samples were programmed to their respective strains. This was determined by observing the recovery of the unstretched shape when heated above

the nematic-isotropic transition temperature (T_{ni}) and returning to the respective programmed strain states when cooled back down to room temperature. The LCE sheets were stored at room temperature in the dark until mechanical testing.

2.2. Wide-angle X-ray scattering (WAXS)

Wide-angle X-ray scattering was performed to quantify the order parameter for polydomain, 30% strain, and 90% strain specimens. The phase of the LCE specimen at room temperature was characterized by a Philips diffractometer (PANalytical, Almelo, Netherlands) using a Philips Copper target (PW-2233/20) with the wavelength of 0.154 *nm*. The beam size was 0.7 x 0.7 mm^2 with flux of 4×10^9 X-ray/s. The distance between the sample and the imaging area was 100 *mm*. The samples were approximately $0.5 \times 6.5 \times 20$ mm^3 and were exposed to the X-ray source for 20 seconds. The data collected by the diffractometer was processed using Image Pro (Media Cybernetics, Inc., Rockville, MD, USA) to obtain the WAXS pattern of scatter intensity and the angular distribution of scatter intensity. The distribution of scatter intensity was smoothed using Igor Pro (WaveMetrics, Inc., Portland, OR, USA) to calculate the order parameter. The angular distribution plots were imported into MATLAB and normalized, such that the integrated intensity from 0 to π would be the range of 0 to 1, and used to calculate the order parameter for the LCE networks using the Kratky analysis method [29] and procedure described by Sims *et al.* [30].

2.3. Dynamic mechanical analysis (DMA)

DMA was performed to determine the onset glass transition temperature T_g^{onset} and the nematic-isotropic transition temperature T_{ni} of the LCE networks using a dynamic mechanical analyzer (TA Instruments, Q800, New Castle, DE, USA). The T_{ni} in this study was defined as the temperature at which the specimens were no longer in the nematic region. Above this temperature, the specimens could be either isotropic or paranematic depending on the method of synthesis. Specimens measuring approximately $16 \times 2.5 \times 1.7$ mm^3 were cut from the programmed sheets for the polydomain and programmed networks. Specimens from the programmed sheets were cut from the middle, either parallel or perpendicular to the director of alignment. Before testing, all specimens were thermally cycled in an oven at 150°C for 5 minutes and then cooled at room temperature for 5 minutes. A dynamic temperature sweep test was performed to measure the temperature-dependent storage modulus. The specimen was equilibrated at 150°C then cooled to -30°C at 2°C/min. The specimen was subjected to 1Hz sinusoidal strain loading of amplitude 0.2%. The T_g^{onset} was defined using the onset intersect function in the TA Universal Analysis software, which finds the temperature at the intersection of a line tangent to the glassy plateau and a line tangent to the middle of the linear drop of the storage modulus. The T_{ni} was approximated as the temperature at the distinct dip in the storage modulus, which is a hallmark of the dynamic soft elasticity behavior of LCEs. Previous studies have shown that the dip in the storage modulus occurs a few degrees below the nematic-isotropic temperature identified by dynamic scanning calorimetry (DSC) measurements [8]. DSC was not used to measure the effects of alignment on T_{ni} or T_g because the reversible shape change of the programmed specimens caused the cross-sectional area in contact with the DSC pan to change during heating and cooling, generating noise and making the results difficult to analyze.

2.4. Uniaxial tension tests

2.4.1. Specimen preparation

Specimens for uniaxial tension tests were prepared by cutting 6 mm wide strips from the center and along the full length of the LCE sheets. Strips were cut either parallel or perpendicular to the direction of the applied pre-stretch and one specimen was prepared from each sheet. A central 30 mm long gage section was marked on the strips by two hand-drawn lines using a black permanent marker. The specimen was gripped at the two black lines and the lines were used to monitor for slippage from the grips during testing. In addition, we marked a smaller 6-10 mm long section in the center of the gage section using 2 black lines and drew in a random speckling pattern for 3D-DIC. The two lines defining the central section were used also to estimate the error for the average DIC displacement and strain measurements. The length of the central section was chosen to prevent the section from stretching beyond the camera field of view during testing. The specimens were heated to 125°C, well above T_{ni}, for 5 minutes in an environmental chamber (Thermcraft Incorporated, Winston Salem, NC, USA) with a temperature controller then cooled at room temperature for at least 15 minutes. The width and thickness of the strips were measured at 3 locations using an electronic caliper (Pro-Max, Fowler, Newton, MA, USA) giving 6.1 mm$\pm$0.70 mm and 0.63 mm$\pm$0.16 mm for the average width and thickness over all the specimens. The specimens were stored at room temperature in the dark.

2.4.2. Fixturing scheme and loading regimen

Uniaxial tension load-unload tests were performed at different strain rates in an MTS Insight 5 equipped with a 500 N load cell (Eden Prairie, MN, USA). The specimens were thermally rejuvenated before testing by heating to 125°C for 5 minutes then cooled at room temperature for at least 15 minutes. The specimen was mounted in tensile screw grips between the 2 lines marking the gauge section. The surfaces of the grip sections were coated with various cyanoacrylate and epoxy adhesives or wrapped in an adhesive tape to increase friction and adhesion with the grips. Tightening the grips caused the specimens to buckle slightly and the cross-head was displaced manually to straighten the specimen by visual inspection. The resulting force was recorded to ensure that it was below a threshold value of 0.06 N, which was determined by monitoring the fluctuations of the MTS load cell reading at zero load. The load cell was zeroed to start the test.

The specimens were subjected to a displacement controlled load-unload test at different engineering strain rates ranging from 0.01%/s to 10%/s. One specimen was prepared for each LCE networks and orientation, except for the 30% parallel, and used for tests at all strain rates to reduce the effect of specimen to specimen variability. Two specimens were used for the 30% parallel tests because the specimen broke during testing. To assess the repeatability of the measurements, we repeated the tests for all strain rates for the polydomain specimen and for the faster strain rates for all other specimens, except the 90% perpendicular, 3-6 times over the duration of the study. 90% perpendicular samples are less likely to have variability due to the increased stiffness. The specimens were thermally rejuvenated before each test. The specimens for different LCE networks structures were stretched to different strain levels to measure as much as possible the nonlinear stress response without breaking the specimen. The polydomain and 30% and 90% pre-stretched perpendicular specimens were stretched to 150%, 300% and 550% strain respectively to fully characterize the semi-soft stress response. The 30% and 90% pre-stretched parallel specimens were stretched to 120% and 50%.

2.4.3. Analysis of Stress Response

A 0.06 N preload was used to set the reference length of the gauge section and the force and displacement measurements where shifted to zero accordingly. The engineering stress was calculated as the force divided by the undeformed cross-sectional area and the engineering strain was calculated from the applied displacements normalized by the reference length. The Young's modulus was calculated from the slope of the stress-strain curve for the small strain range of 0.0 - 0.1. The hysteresis was calculated by numerically integrating the area under the load-unload engineering stress-strain curve using the trapezoidal rule.

The polydomain and monodomain specimens loaded perpendicular to the alignment direction exhibited a soft stress response caused by domain/mesogen rotation. The limits of the soft stress region were determined by first locating the minimum stress in the region. Starting from this point, the local slope of the stress-strain curve was calculated to the left and right of this point by fitting a line to a small neighboring group of 5 points. The begin and end strains were located when the slope on either side reached 20% of the Young's modulus. Using this criteria, the beginning strain coincided with the peak stress for most cases.

2.4.4. 3D Digital Image Correlation

The specimen was imaged during testing using a stereoscopic system consisting of 2 monochrome cameras (GRAS-20S4M-C, Point Grey, Richmond, BC, Canada) with 2 megapixel resolution, $11.84^\circ \pm 3.95^\circ$ stereo-angle, and 35 mm objective (Xenoplan 1.9/35 mm-0901, Schneider Optics, Hauppauge, NY, USA). The specimen was illuminated by a circline light bulb (90922L, Commercial Electric, Cleveland, OH, USA) and diffused light from incandescent lamps placed behind white sheets of paper. The images were acquired by Vic-Snap 2009 (Correlated Solutions Inc., Columbia, SC, USA) and the acquisition rate was varied to acquire 100 pictures during the load-unload tests. The images were imported into Vic-3D 2012 (Correlated Solutions Inc., Columbia, SC, USA) for DIC analysis of the 3D displacement field. A large, 25×25 pixels, subset size and incremental correlation method were used because the speckles became greatly distorted at large strains. In incremental correlation, the image at each time step was compared to the preceding image to calculate the incremental displacement field. The in-plane components of Green-Lagrange strain field, E_{yy}, E_{xx}, and E_{xy}, were evaluated by Vic-3D using the default interpolation and smoothing settings. The y and x directions denote the loading (axial) and transverse directions, respectively. The Green-Lagrange strain tensor is defined from the deformation gradient $\mathbf{F} = \mathbf{I} + \nabla \mathbf{u}$ as, $\mathbf{E} = \frac{1}{2}\left(\mathbf{F}^T\mathbf{F} - \mathbf{I}\right)$, where $\mathbf{I}$ is the identity tensor

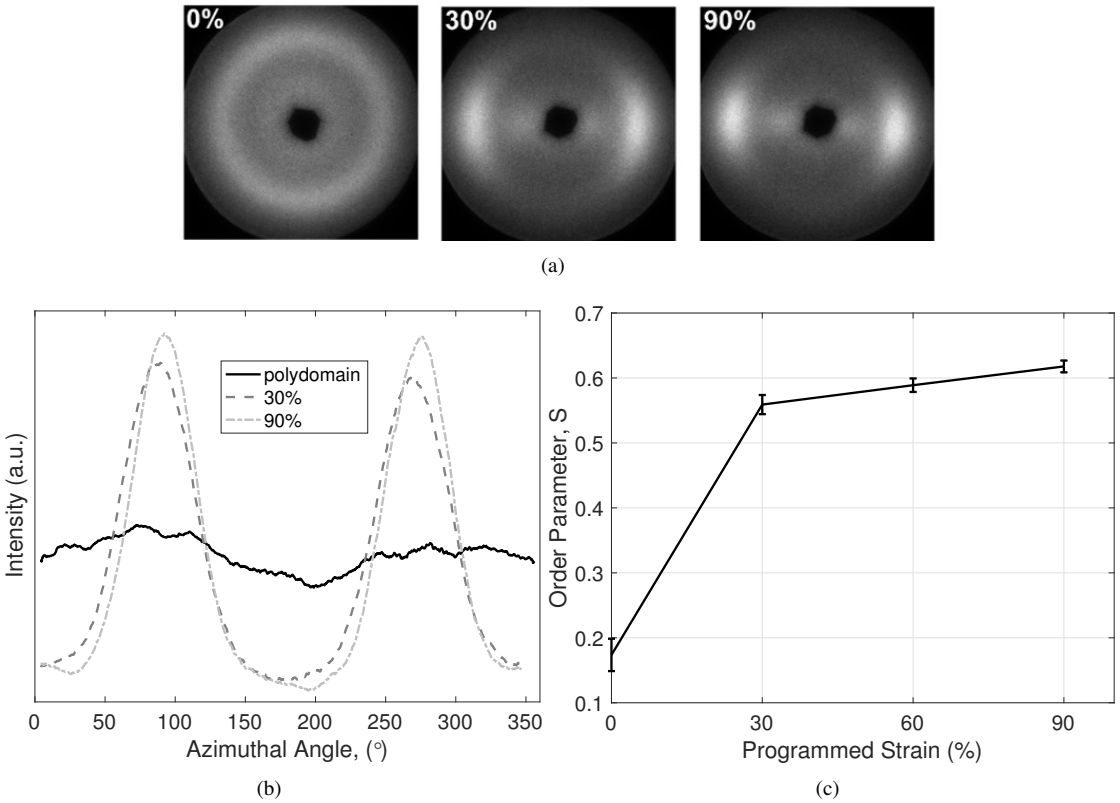

Figure 1: Analysis of (a) the WAXS pattern to obtain (b) the angular distribution of scatter intensity, plotted for representative specimens of networks programmed at 0% strain (polydomain), 30% strain, and 90% strain, and (c) the order parameter for mesogen alignment for LCE networks programmed at different strains. Plotted are the average and standard deviation of the order parameter of 3 specimens for each programmed strain. The peak intensity in the WAXS pattern and the angular distribution plots and the order parameter showed a sharp increased from 0% to 30% programmed strain and a smaller increase at 90% programmed strain.

and $\mathbf{u}$ is the displacement vector. The axial and lateral strain components can be related directly to the axial stretch λ_y and lateral stretch λ_x as, $E_{yy} = \frac{1}{2}\left(\lambda_y^2 - 1\right)$ and $E_{xx} = \frac{1}{2}\left(\lambda_x^2 - 1\right)$.

3. Results and Discussion

3.1. Wide-angle X-ray scattering

The WAXS pattern for the LCE polydomain exhibited a circular shape with a circumferentially uniform intensity, while the WAXS patterns for the pre-stretched networks featured lobes of higher scatter intensity at orientations corresponding to the director orientation (Figure 1a). The brightness of the lobes increased with the programmed strain. The WAXS patterns clearly showed that the initially nearly uniform distribution of scatter intensity evolved into increasingly sharper peaks with increasing programmed strain (Figure 1b). The order parameter jumped from 0.17 for the polydomain specimen to 0.56 for the 30% pre-stretched specimen, which retained an opaque appearance. The order parameter for the 90% pre-stretched specimen was slightly higher at 0.62, though the specimen appeared transparent. The increase in the order parameter with programmed strain agreed with previous WAXS measurements for main-chain nematic LCEs. Bergmann *et al.* showed that an unstrained main-chain LCE polydomain network exhibited a low, near-zero, order parameter. Stretching the sample caused the order parameter to increase rapidly in the soft stress region, as the mesogens become increasing aligned, to a plateau value of less than 0.8 [31]. Recent studies by Ware *et al.* [25] and Saed *et al.* [27] also reported WAXS measurements showing a non-zero order parameter for polydomain main-chain LCEs. The residual non-zero order parameter found in the polydomain specimens from

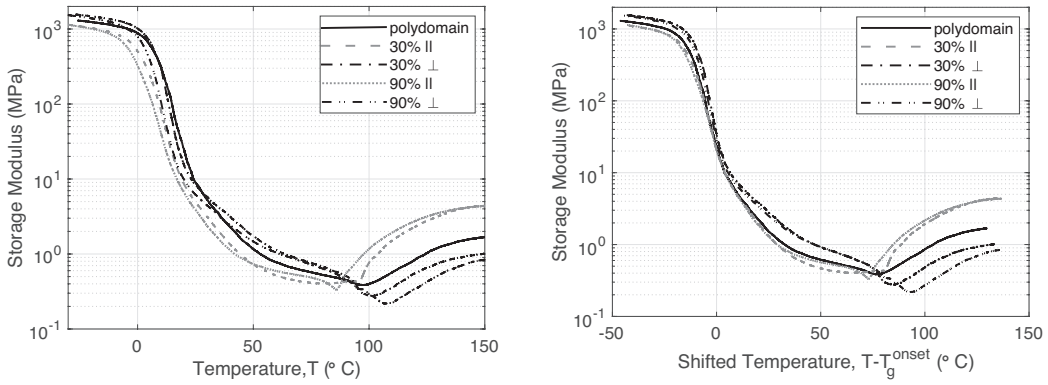

(a) (b)

Figure 2: The temperature dependence of the uniaxial tensile storage modulus plotted with respect to (a) temperatures and (b) temperature relative to the onset glass transition temperature T_g^{onset} for the polydomain and programmed networks measured in the perpendicular ($\perp$) and ($\parallel$) directions.

this study could be explained by two possible experimental limitations. First, the X-ray beam size was 0.7 mm $\times$ 0.7 mm. The small beam size may have prevented the beam from sampling a sufficiently large number of domains to measure an averaged random orientation. The domain size for polydomain networks crosslinked in the nematic state have been measured in the tens of microns [16]. Second, the samples were compliant, such that mounting the specimens onto the platform may have induced a small strain resulting in a slight initial orientation.

3.2. Dynamic mechanical analysis

The storage modulus of the LCE networks plotted with respect to the temperature (T) and the temperature relative to the onset glass transition temperature $T - T_g^{onset}$ are shown in Fig. 2. Table 1 lists for all networks the T_g^{onset} and T_{ni} calculated from the temperature-dependence of the storage modulus (Sec. 2.3), as well as the storage modulus at 22°C (room temperature) and at $T_{ni} + 40$°C. The T_g^{onset} decreased slightly with increasing applied pre-strain, and was 4°C lower for specimens tested in the parallel than in the perpendicular direction. The storage modulus for all specimens exhibited a dip at T_{ni}, which is characteristic of dynamic soft elasticity. By shifting the storage modulus curves relative to the T_g^{onset} of each specimen (Figure 2b), the difference in the temperature range between the glass transition and nematic-isotropic transition became more apparent when comparing the polydomain and programmed networks. Programmed specimens tested parallel to the director had a smaller temperature range $T_{ni} - T_g^{onset}$ than those tested perpendicular to the director. The storage modulus for the programmed specimens tested in the parallel direction also showed a dip at T_{ni} that may have been caused by the rotation of the remaining unaligned domains towards the loading direction. A larger dip in the storage modulus was measured for the programmed specimens tested in the perpendicular direction. Previous DMA studies of the viscoelastic behavior of LCEs compared the storage modulus measured by shear applied parallel to the director and in a plane perpendicular to the director, and found that the storage modulus in the perpendicular direction did not exhibit a dip at T_{ni} [23, 20, 32]. The director is not coupled to the network deformation for shearing in a plane perpendicular to the director. This is contrast to the uniaxial tensile loading applied in the perpendicular direction in this study, which would cause the director to rotate towards the loading direction. Both the dip in the storage modulus and the temperature range $T_{ni} - T_g^{onset}$ increased with increasing alignment. The storage modulus for all specimens exhibited nearly identical dependence on the relative temperature $T - T_g^{onset}$ up to $T_g^{onset} + 20$°C, after which the programmed networks loaded in the perpendicular direction showed a more gradual decrease with temperature. At higher temperatures, mesogen relaxation may contribute to broadening the relaxation spectrum for the viscoelastic behavior of the networks.

The storage modulus at 22° C was lower in the more aligned specimens with lower glass transition temperatures. The rubbery storage modulus for the programmed networks were larger in the parallel than perpendicular directions. At $T_{ni} + 40$°C, the mesogens have lost their nematic ordering and programmed alignment. The anisotropy in the

Specimen	Direction	T_g^{onset} (°C)	T_{ni} (°C)	$T_g^{onset} - T_{ni}$ (°C)	E'@22° C (MPa)	E'@T_{ni} + 40° C (MPa)
polydomain (0%)	–	8.0	97.1	89.1	15.4	1.4
30%	∥	2.3	88.5	86.2	6.7	3.8
30%	⊥	6.2	101.1	94.9	11.4	0.9
90%	∥	-1.5	85.7	87.2	4.9	3.2
90%	⊥	2.7	108.4	105.7	8.0	0.8

Table 1: Thermomechanical properties of the LCE networks programmed at different pre-strained and tested parallel and perpendicular to the alignment direction. E denotes the storage modulus measured at different temperatures.

storage modulus may be caused by the programed chain alignment. However, the rubbery storage modulus for the 30% and 90% pre-stretched specimens were nearly identical both in the parallel and perpendicular directions.

3.3. Rate-dependent uniaxial tension response

The rate-dependent stress-strain curves from representative load-unload uniaxial tension tests for the different LCE networks are shown in Fig. 3. The stress response did not show a systematic variation between the repeated tests (e.g., the specimens did not stiffen after each test) because the materials were thermally cycled prior to testing, and the variations between the repeated tests were smaller than between the different strain rates (Supplemental Figs. 1-5). All LCE networks structures exhibited a rate-dependent stress response and inelastic strain upon unloading. The inelastic strain did not recover after unloading at room temperature, but full recovery was observed after heating the specimen above T_{ni}. Previously, Azoug *et al.* [9] reported full strain recovery after 2-15 minutes at room temperature for a polydomain with a higher content of reactive acrylate groups (15 mol% in excess of the thiol groups) than the polydomain used here, which only contained 2 mol% of excess acrylate groups, resulting in a lower crosslinked density.

As expected, the polydomain and programmed networks loaded in the perpendicular direction exhibited a soft stress response from domain/mesogen rotation towards the loading direction, characterized by a linear region, peak stress, strain-softening and strain-hardening (Fig. 3a, d, e). For the 90% perpendicular specimen loaded at 0.01%/s, we did not detect a linear region and it may have occurred below the force threshold. The soft stress response of the polydomain at different strain rates did not merge after the polydomain-monodomain transition and remained rate-dependent even after the specimen became transparent (Fig. 3a), which differed from the observations of Clarke *et al.* [6] for a siloxane side-chain polydomain. Stretching the highly aligned 90% pre-stretched networks in the parallel direction also produced a rate-dependent stress response (Fig. 3c). The stress response for the 90% perpendicular specimen also remained rate-dependent well beyond the soft stress region, after the mesogens were align with the loading direction (Fig. 3e). Altogether, these observations suggested that the relaxation dynamics of the network contributed significantly to the rate-dependence and hysteresis of the stress response in these materials.

3.3.1. Young's modulus

The Young's modulus for all networks structures increased linearly with the strain rate on a log-log plot in Fig. 4a, indicating a power-law relationship. The power-law exponent was determined by fitting a line to the log-log plot of the Young's modulus averaged over all the repeated tests. We were unable to calculate the Young's modulus for the 90% perpendicular specimen at 0.01%/s, because the stress response did not show a linear region. The Young's modulus of the 30% pre-stretched networks showed the most rate-dependence with a power-law exponent m ranging between 0.36-0.39, followed by the polydomain with a slightly smaller $m = 0.31$. The 90% pre-stretched networks showed a noticeably weaker rate-dependence, with a power-law exponent of $m = 0.22$ for the parallel direction and $m = 0.15$ for the perpendicular direction. As a result, the modulus for the 90% perpendicular specimen increased by a factor of 2 from 0.1/s to 10/s, while the modulus for the polydomain increased by factor of 6 over the same range of strain rates. The modulus also increased with the applied pre-stretch and was greater in the parallel than perpendicular direction for the 90% pre-stretched networks. The modulus in the parallel direction, $E_{\parallel}$, of the 90% pre-stretched networks was at most 2 times larger than the modulus in the perpendicular direction, $E_{\perp}$, but it was on average 5 times larger than

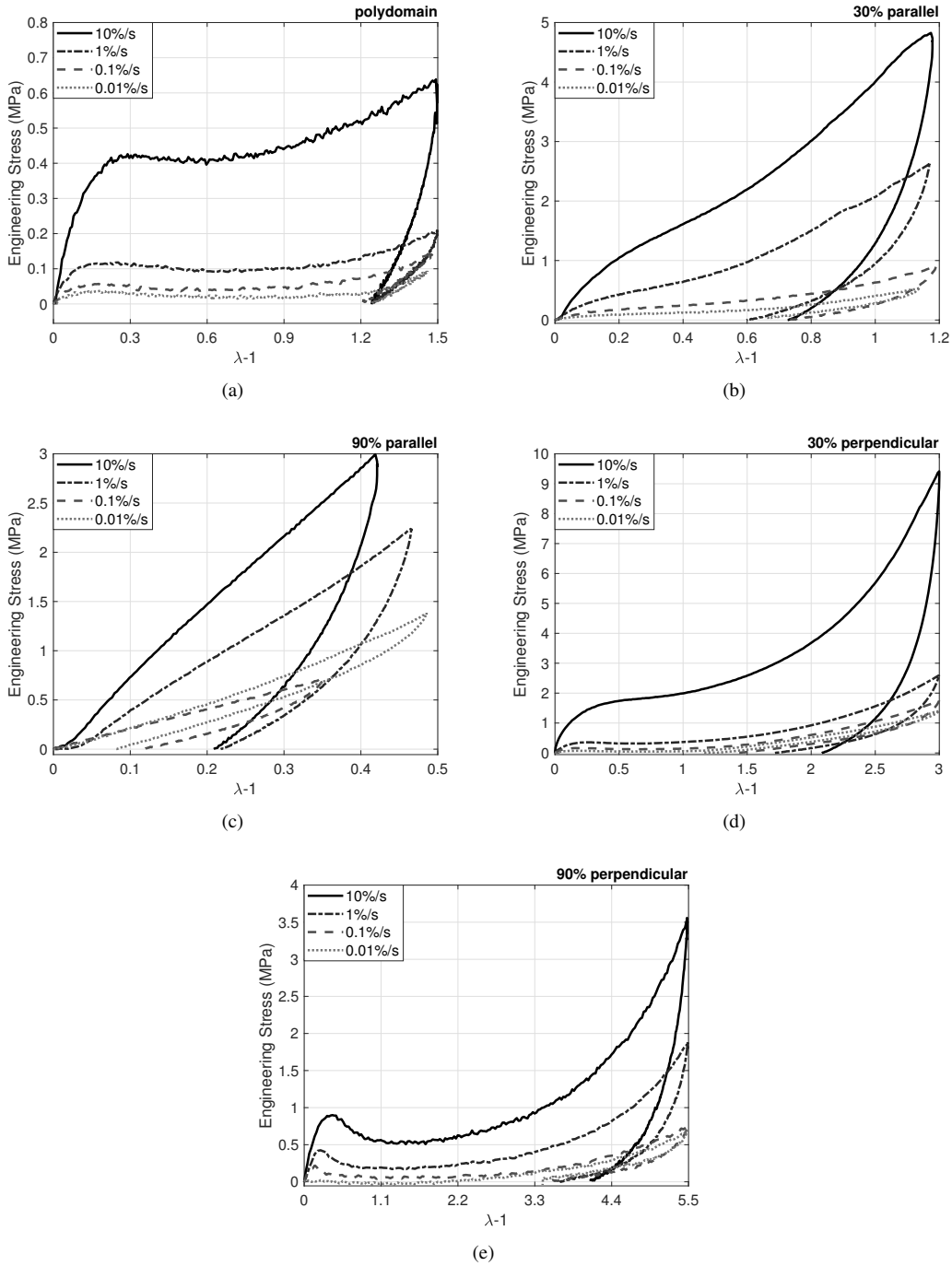

Figure 3: Uniaxial tension load-unload stress-strain response for representative tests at strain rates 10%/s, 1%/s, 0.1%/s, and 0.01% for different pre-stretched LCE networks and loading directions relative to the pre-stretched direction: (a) 0% polydomain, (b) 30% parallel, (c) 90% parallel, (d) 30% perpendicular, and (e) 90% perpendicular. The specimens for different LCE networks were stretched to different strain levels to measure as much as possible the nonlinear stress response without breaking the specimen. All LC networks exhibit a rate-dependent stress response with inelastic strain at unloading.

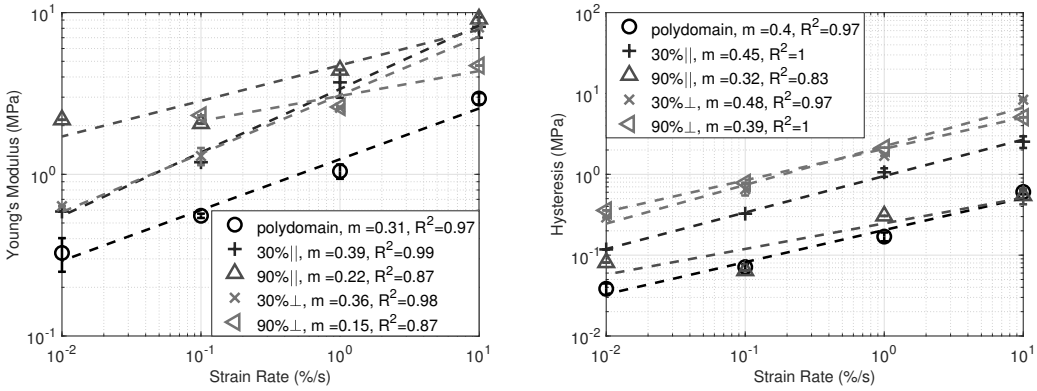

(a) (b)

Figure 4: The rate-dependence of (a) the Young's modulus and (b) the hysteresis of the uniaxial tension engineering stress-stretch curves for different pre-stretched LCE networks and loading directions relative to the pre-stretched direction: 0% polydomain, 30% parallel, 90% parallel, 30% perpendicular, and 90% perpendicular. Plotted are the average over all repeated tests and the error bars indicate the variation between repeated tests. The slope (m) in a log-log plot gives the power-law rate-dependence. A larger pre-stretch produced a higher Young's modulus and weaker rate-dependence.

the modulus of the polydomain. For the 30% pre-stretched networks, the $E_{\|}$ was slightly higher than $E_{\perp}$ for the 1%/s and 10%/s strain rates but were nearly identical for the lower strain rates. The ratio of $E_{\|}/E_{\perp}$ measured for the 90% pre-stretched networks was consistent with the storage modulus measurements at room temperature (Table 1) and with previous measurements of Merkel *et al.* [21], which also reported a ratio of $E_{\|}/E_{\perp} = 2$ for the same acrylate content and pre-stretch. However, the ratio $E_{\|}/E_{\perp} = 2$ measured for the 30% pre-stretched was significantly smaller than the ratio for the storage modulus measurements at room temperature. Moreover, the Young's modulus generally increased with the programmed pre-strain, while the storage modulus measured at room temperature showed the opposite trend because alignment lowered the glass transition temperature. The Young's modulus was calculated for a larger strain range (0-10%) in the uniaxial tension than the storage modulus, which may lead the different dependence on the alignment.

3.3.2. Hysteresis

The load-unload stress response for all LCE networks exhibited significant hysteresis that increased with the strain rate according to a power-law relation (Fig. 4b). It should be noted that the hysteresis depends on the maximum strain applied in the load-unload test. The specimens were stretched to different strain levels to characterize the nonlinear features of the soft stress response, which for the polydomain and perpendicular specimens included the effects of domain/mesogen rotation and relaxation. In general, the hysteresis was larger for the stress response of the programmed networks than for the polydomain. For the programmed networks, the hysteresis was larger in the perpendicular direction than parallel direction. The rate-dependence did not vary systematically with the programmed stretch. The power-law exponent was highest for the 30% prestretched networks, varying from $m = 0.45 - 0.48$ and smallest for the 90% pre-stretched networks, with $m = 0.32$ for the parallel and $m = 0.39$ for the perpendicular directions. The polydomain had a similar $m = 0.4$ For the programmed networks, the hysteresis in the perpendicular direction had a slightly stronger rate-dependence than in the parallel direction. However, the differences with alignment and loading direction were smaller for the hysteresis than the Young's modulus (Fig. 4a).

3.4. Soft stress region

The peak stress for the polydomain and programmed networks stretched in the perpendicular direction increased with increasing strain rate according to a power-law relation, with an exponent between $m = 0.35 - 0.46$ (Fig. 5a). There was no systematic variation of the power-law exponent with the pre-stretch. The exponent was largest for the

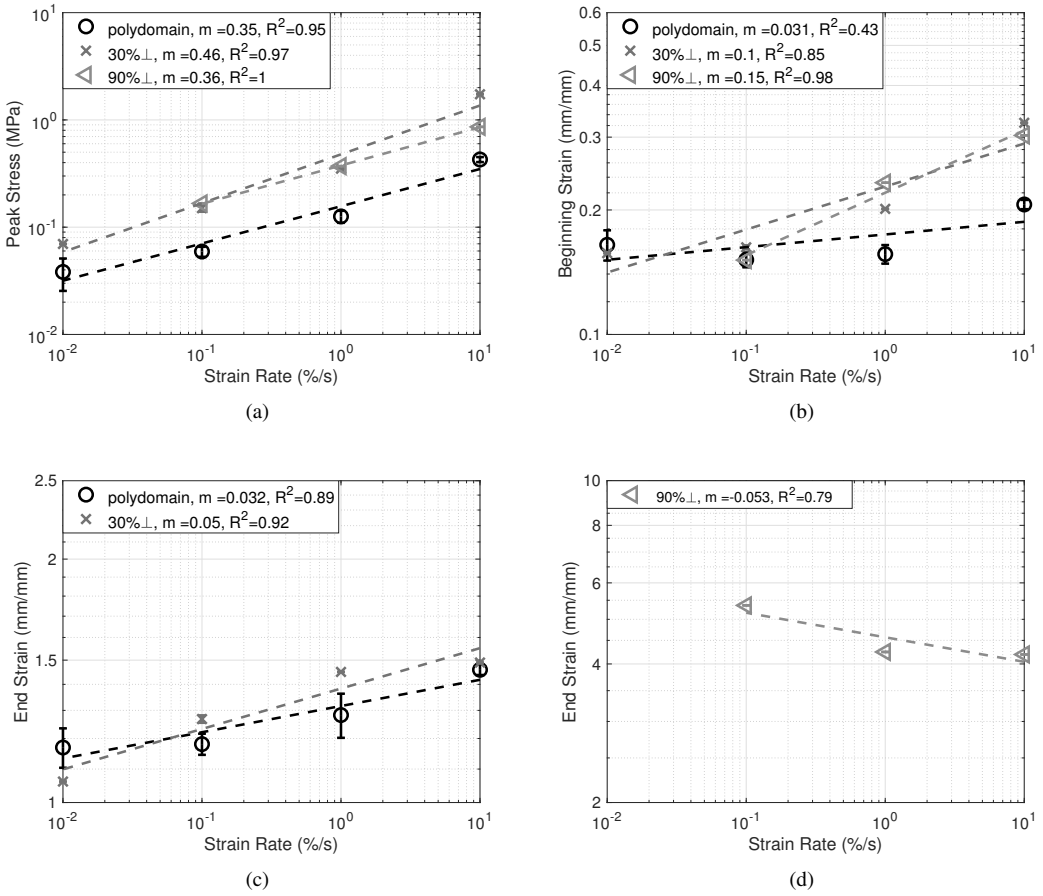

Figure 5: Characteristics of the rate-dependent soft stress response for 0% polydomain, and 30% and 90% pre-stretched networks loaded perpendicular to the pre-setrecth direction, showing: a) the peak stress for all specimens, (b) the beginning strain for all specimesn, c) the end strain of the polydomain and 30% perpendicular specimen, and d) the end strain of 90% perpendicular specimen. The error bars show the variation for all repeated tests. The slope (m) of the linear fit in a log-log plot gives the power-law rate-dependence. The peak stress increased with strain rate for all networks structures while the beginning and end strains were less sensitive to strain rates.

30% pre-stretch and smallest for the polydomain. The stress magnitude for 30% pre-stretched and 90% pre-stretched networks were approximately 2 times the polydomain stress response.

The beginning strain and end strain of the soft stress response were less sensitive to the strain rate, with power-law exponents varying from $m = 0.03 - 0.15$ (Fig. 5b-d). Alignment increased the rate-dependence of the beginning strain. The end strain for the polydomain and 30% pre-stretched networks increased with increasing strain rate from 110% to 150%, while the end strain for the 90% pre-stretched networks decreased from 5.5 to 4. The relaxation dynamics of the domains/mesogens and networks chains both influence to the slope of the soft stress response. Whether the begin and end strains of the soft stress region increase or decrease with the strain rate may depend on the relative contributions of domains/mesogens relaxation and chain relaxation to the stress response.

3.5. 3D-DIC strain measurements

Color contour plots of the axial Green-Lagrange strain E_{yy} and shear strain E_{xy} from representative tests measured by 3D-DIC at 1%/s strain rate for the different LCE networks at the maximum stretch are shown in Figure 6. The strains are normalized by the maximum applied Green-Lagrange strain. The axial strains were non-uniform for all networks (Fig. 6a) and significant shear strains developed in the 30% parallel and 90% parallel specimens (Fig. 6b).

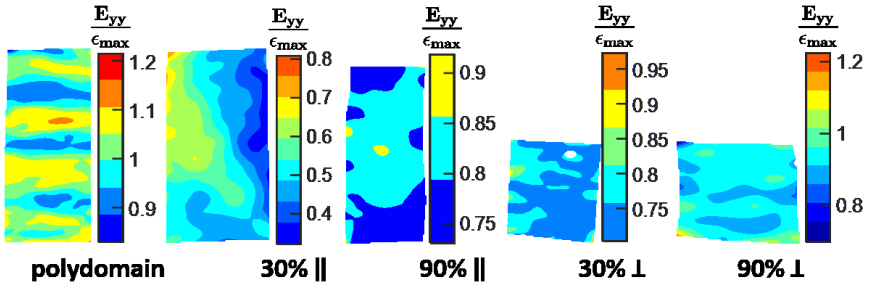

(a)

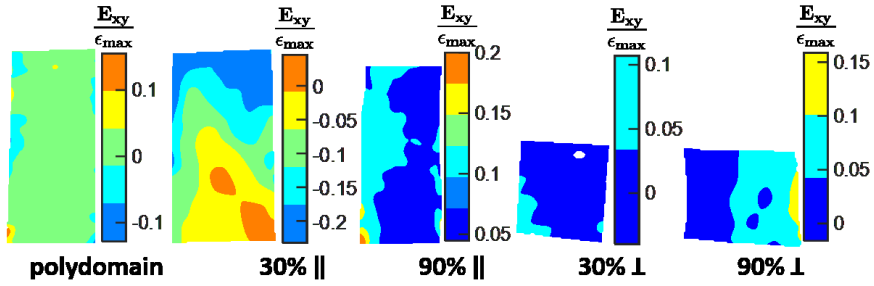

(b)

Figure 6: Strain contours for the Green-Lagrange axial strain E_{yy} (a) and for the Green-Lagrange shear strain E_{xy} measured using 3D DIC for representative uniaxial tension tests at the maximum applied stretch and 1%/s strain rate. The strains are normalized by the maximum applied axial Green-Lagrange strain ε_{max} for the specimen and plotted over the undeformed configuration to more effectively visualize the spatial variation. The axial strains were nonuniform in all specimens. Shear strains developed in the 30% parallel and 90% parallel specimens.

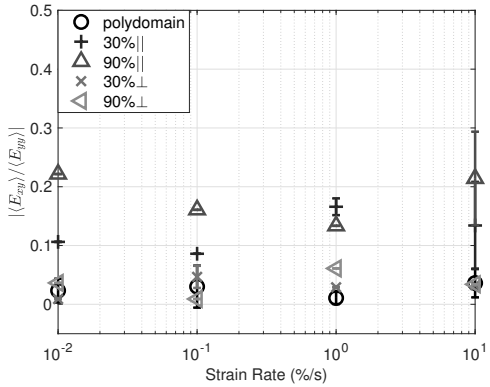

Figure 7: The ratio of the specimen-averaged Green-Lagrange shear strain E_{xy} and specimen-averaged axial strain E_{yy} measured by 3D DIC as a function of strain rate for different LCE pre-stretched networks and loading directions: 0% polydomain, 30% parallel, 90% parallel, 30% perpendicular, and 90% perpendicular. The strain ratio was calculated from the slope of a line fit to a plot of the specimen-averaged E_{xy} vs. E_{yy} for every 10% interval in the applied strain during loading. The error bars show the variation in the strain ratio computed for all applied strain intervals applied stretch and all repeated tests. Loading parallel to the pre-stretch direction induced significant shear strains that increased with the pre-stretch.

The spatial variation for E_{yy} showed alternating horizontal bands of higher and lower axial strains for the polydomain, 30% perpendicular, and 90% perpendicular specimens that experience domain/mesogen rotation during loading, while diagonal bands of shear and axial strains developed in the 30% parallel specimen (Fig. 6a). The patterns appeared consistently in all repeated testing of the specimens. Two 30% parallel specimens were tested because one broke during the course of the experiment and the diagonal strain pattern appeared for both specimens.

3.5.1. Shear Strain

The ratio of the averaged shear to axial strain was calculated by plotting the specimen-averaged E_{xy} versus the specimen-averaged E_{yy} and fitting a line to the plot for each loading interval. The ratio of the shear to axial strains were averaged over all strain intervals and repeated tests and plotted in Fig. 7 to compare the effects of strain rate and degree of alignment. The polydomain and 30% perpendicular specimens experienced negligible shear strain relative to the axial strain, while the 90% parallel specimen experienced the highest ratio of shear strain to axial strain, followed by the 30% parallel specimens. The standard deviation in the ratio of shear to axial strains was small for nearly all specimens, which indicated that the shear and axial strain patterns developed together in such a way that their ratio remained unchanged over a wide range of strains during loading. The presence of shear strains in the programmed specimens but not in the polydomain suggests that the shear strain patterns were caused by an initially nonuniform mesogen microstructure in the programed specimens. During programming, polydomain samples were stretched, producing a nonuniform mesogen microstructure (as evidenced by the nonuniform strain field in Fig. 6), which were locked in by the subsequent crosslinking step. Previous studies of uniaxial tension tests of monodomains have shown that the applied stretch causes misaligned mesogens to rotate towards the loading direction. This caused the development of local microstructures, such as vertical stripe domains of alternating positive and negative shears away from the clamps and more disordered microstructures near the clamps [33, 34], producing shear strains and a non-uniform strain field [35]. In this study, the resolution of the DIC measurements were too large to detect features of stripe domains and further microstructural characterizations, e.g., using WAXS [33] or FTIR [34], and computational modeling studies are needed to determine the underlying domain microstructure of the strain patterns.

3.5.2. Axial Strain

To further investigate the development of the heterogeneities in the axial strain, we plotted E_{yy} at different points in the soft stress region for the polydomain at different strain rates (Fig. 8). Similar plots, showing the development of strain heterogeneities at different points in the soft stress region for all the LCE networks are shown in the Supplemental Figs. 6-8. For the lower strain rates, the axial strain appeared uniform until the onset of the soft stress response,

where a horizontal band of higher strain developed in the middle of the specimen (Fig. 8c,d). A diagonal band of lower strain appeared during strain-softening and a pattern of alternating bands of higher and lower strains emerged during strain-stiffening. These observations suggest that the strain bands formed from local relaxation of the domain orientation, which led to stress relaxation, more specifically, to the strain-softening portion of the stress response. At faster strain rates, the onset of the soft stress response did not coincide with the appearance of strain localization and heterogeneities in the axial strain (Fig. 8a,b), which suggests that the domains rotated uniformly as predicted and did not have sufficient time to relax and reorient to a lower energy state. As a result, the stress response at the higher strain rates did not exhibit noticeable strain-softening after the peak stress, and the soft stress region appeared more like a plateau before strain-stiffening (Fig. 3a). Heterogeneities in the strain field eventually developed near the end of the loading curve, when enough time had passed for domain relaxation to occur (Fig. 8a,b).

To quantitatively characterize the development of strain heterogeneities, we calculated the standard deviation of the Green-Lagrange axial strain normalized by the average strain measured by 3D-DIC for the loading portion of representative tests at different strain rates (Fig. 9). The standard deviation generally increased with the strain in all cases, and normalizing by the average strain showed more clearly how the variations grew relative to the average strain. The initial high normalized variation may have been caused by heterogeneities induced by the programed pre-strain or by dividing by small strain values. For the 90% parallel specimen, the normalized strain variation decreased continuously with strain to about 5% at the maximum strain (Fig. 9c). The normalized strain variation also decreased initially for the polydomain and programmed specimens loaded in the perpendicular direction, but then increased near the onset of strain-softening in the stress response to a maximum value before decreasing back to 5% or less during strain-stiffening at end of the soft stress region (Fig. 9a,d,e). The variations in this region were caused by local domain/mesogen relaxation that led to the formation of strain bands in Fig. 8c,d. For the polydomain and 30% perpendicular specimens, the strain variation increased with decreasing strain rate and were less than 5% of the strain (essentially negligible) for the fastest strain rate (Fig. 9a,d). The strain variation for the 30% parallel specimen also showed a gradual increase after an initial decrease and a larger increase in variability was measured for lower strain rates (Fig. 9b), which may indicate that the 30% pre-stretched specimen also experienced domains rotation and relaxation even when loaded in the parallel direction.

In contrast, the strain variation was less sensitive to the strain rate for the 90% perpendicular specimen. While the strain variation at 10%/s was smaller than at 0.01%/s for the 90% perpendicular specimen (Fig. 9e), the difference in the maximum normalized standard deviation between the two strain rates was an order of magnitude smaller than for the polydomain specimen (Fig. 9a). Moreover, the strain variability evolved over a significantly larger strain range and longer time than for the polydomain and 30% parallel specimens. For the lower 0.01%s strain rate, the strain variability reached a peak at a lower strain than for the polydomain and 30% specimen, then decreased to a constant value up to $E_{yy} = 2$ (Fig. 9f) before gradually decreasing back to 5% of the applied strain (Fig. 9e). These observations indicated that mesogen relaxation in the highly aligned network can occur at shorter times than domain relaxation and is characterized by a broader distribution of relaxation times. This is consistent with the results of the DMA experiments showing a more gradual decrease in the storage modulus near T_{ni} for the perpendicular specimens. Urayama and coworkers [16] also reported that strain recovery occurred faster in monodomain than polydomains. Schonstein *et al.* [36] measured the relaxation of the director in a monodomain using dynamic light scattering and found a broader distribution of relaxation times and a fast mean relaxation time of 0.01 s.

3.5.3. Lateral Strain

The specimen-averaged lateral strain E_{xx} was plotted against the specimen-averaged axial strain E_{yy} in Figure 10 for representative tests of all specimens and strain rates. As expected, the lateral strain E_{xx} decreased (became more negative) with E_{yy}. The relationship between the lateral and axial strain were insensitive to the strain rate, which indicates that the Poisson's ratio was not rate-dependent. The semi-soft elasticity theory [37, 38] was applied to analyze the development of the lateral strain. The theory breaks the semi-soft elastic response for a monodomain stretched perpendicular to the director into three regions. In region 1, where there is no discernable director rotation, and region 3, where the director rotation is complete, the theory predicts that the material should behave like a regular incompressible isotropic elastomer, with a lateral strain $\lambda_x = \lambda_y^{-1/2}$, which corresponds to a Poisson's ratio of 0.5. In region 2, where deformation occurs mainly by director rotation, the theory predicts that $\lambda_x = \lambda_y^{-1}$, which corresponds to a Poisson's ratio of 1. We overlaid the theoretical prediction for $\lambda_x = \lambda_y^{-1/2}$ in all of the plots in Figure 10 and

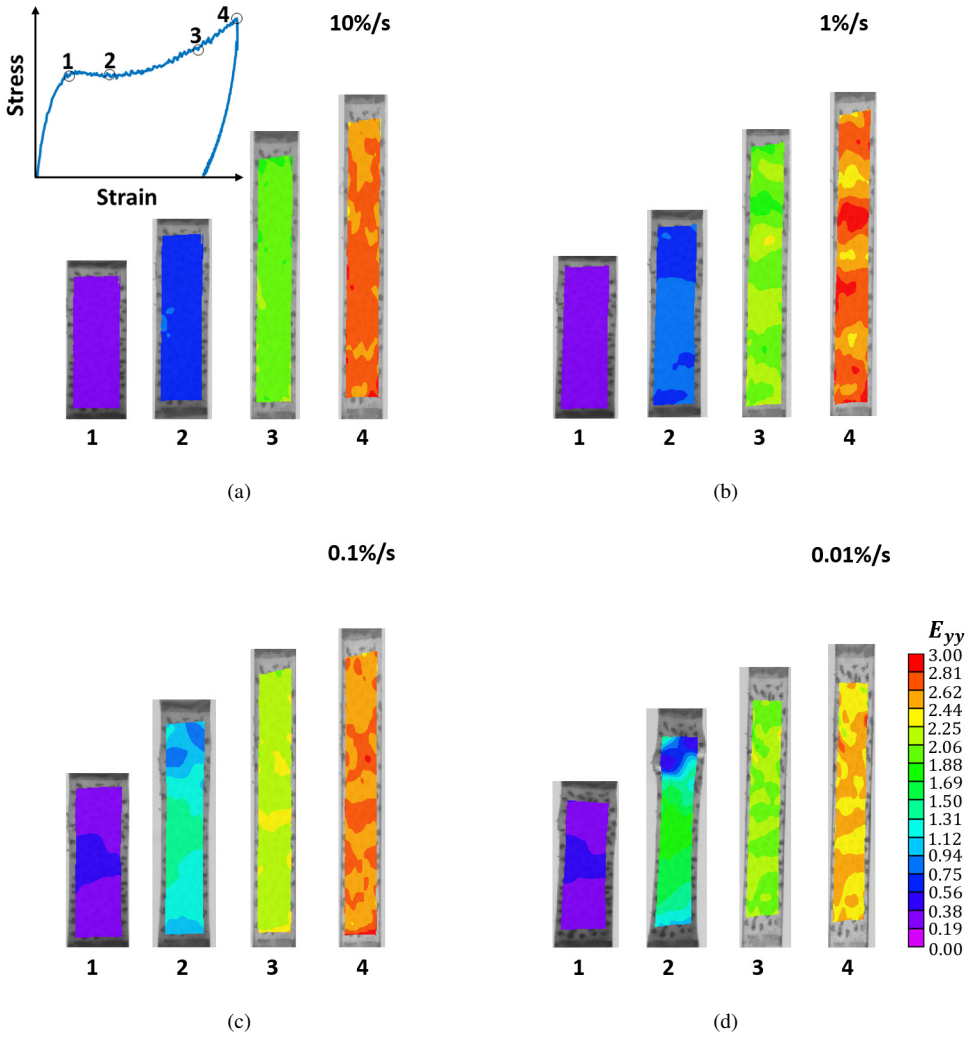

Figure 8: Strain contours for the Green-Lagrange axial strain E_{yy} measured using 3D DIC at 4 points in the soft-stress response for representative tests of polydomain specimens at (a) 10%/s, (b) 1%/s, (c) 0.1%/s, and (d) 0.01% strain rates. The contours are plotted over the deformed specimen. An example of the stress-strain curve is also included to indicate the four points in the soft stress response: 1- the starting point for softening; 2- strain softening; 3-strain hardening; and 4- the maximum stretch.

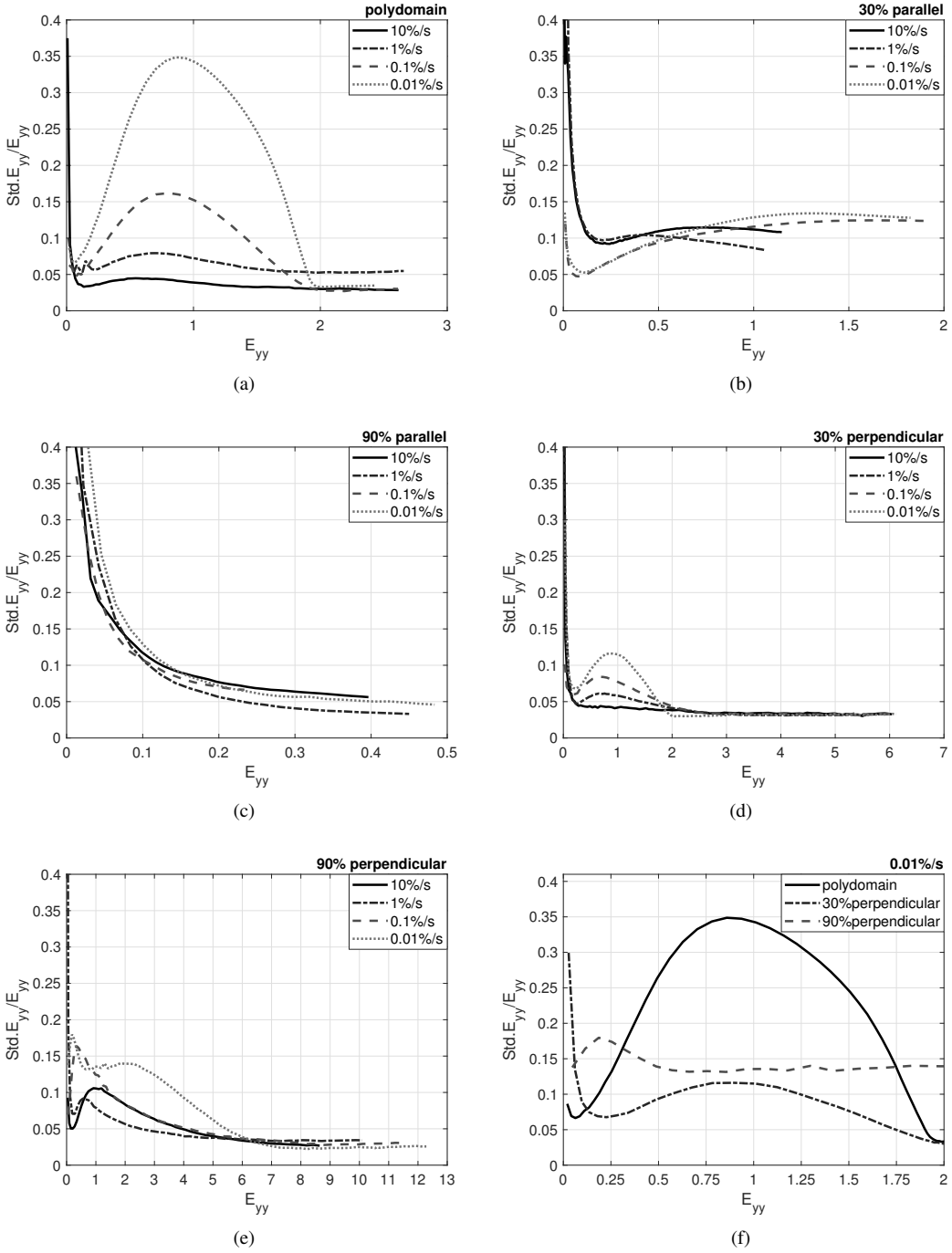

Figure 9: Standard deviation of the Green-Lagrange axial strain E_{yy} from 3D DIC normalized by the specimen-averaged E_{yy} for representative tests at different strain rates for the different LCE networks structures and loading directions: (a) 0% polydomain, (b) 30% parallel, (c) 90% parallel, (d) 30% perpendicular, and (e) 90% perpendicular; and (f) a comparison of the normalized standard deviation of E_{yy} measured for the polydomain, 30% perpendicular and 90% perpendicular specimens at 0.01%/s. For the perpendicular and polydomain specimens, strain variations increases and peaks during soft-elasticity and larger variation is measured for smaller strain rates. The polydomain specimen exhibited the had the highest peak in the strain variations, however the strain variations persisted over a larger strain range for the 90% perpendicular specimen.

the theoretical prediction $\lambda_x = \lambda_y^{-1}$ for the 90% perpendicular specimen in Figure 10e. The E_{xx} measured for the 90% perpendicular specimen agreed well with the theoretical prediction for mesogen rotation, $\lambda_x = \lambda_y^{-1}$. The stress response for the 90% perpendicular specimen began to stiffen with strain around $\lambda_y \approx 4$ and the lateral contraction became increasingly smaller than predicted by $\lambda_x = \lambda_y^{-1}$, indicating a transition to the other $\lambda_x = \lambda_y^{-1/2}$ theoretical limit. Higaki et al. [34] also reported for a side-chain monodomain a larger in-plane Poissons ratio of 0.9 in the soft stress region and an incompressible Poissons ratio 0.5 before and after the soft stress region. The E_{xx} for all other specimens followed the theoretical prediction for an isotropic network, $\lambda_x = \lambda_y^{-1/2}$. Applying 2D-DIC, Pritchard et al. [24] also measured an equilibrium Poisson's modulus of 0.5 for a polydomain LCE.

4. Conclusions

The purpose of this study was to investigate the effect of alignment on the dynamic mechanical behavior, rate-dependent stress response, and mechanical dissipation in main-chain LCEs. 3D-DIC was also applied in the uniaxial tension tests to characterize the effects of mesogen/domain rotation and relaxation on the strain field. The main findings of the DMA and uniaxial tension tests were:

- In DMA tests of perpendicular specimens, the temperature range $T_g^{onset} - T_{ni}$ and the dip in the storage modulus at T_{ni} increased with increasing alignment.
- All specimens exhibited a power-law rate-dependence in the Young's modulus, peak stress, and hysteresis in load-unload uniaxial tension tests.
- The Young's modulus and hysteresis of the 90% pre-stretched specimens exhibited a weaker rate-dependence, with smaller power power-law exponents, than those of the polydomain and 30% pre-stretched specimens.
- The Young's modulus of the 90% pre-stretched specimen in the perpendicular direction was smaller and less sensitive to strain rate than in the parallel direction. For the 30% pre-stretched specimens, the Young's modulus and its rate-dependence were the same in the parallel and perpendicular directions and were also the same as those of the polydomain.
- 3D-DIC showed a highly heterogeneous axial strain field for all specimens and heterogenous shear strain field for all programed specimens. The specimen-averaged shear strain was 20% and 10% of the average axial strain for the 90% and 30% parallel specimens, respectively, but were nearly zero for the polydomain and programmed specimens stretched in the perpendicular direction.
- For the polydomain specimens and programmed specimens loaded in the perpendicular direction, the DIC axial strain field showed the development of local bands of higher and lower strains in the soft stress region. The variation in the axial strain increased during the strain-softening portion of the stress response then decreased during the strain stiffening portion of the stress response.
- Larger strain variations was measured for lower strain rates for the polydomain and programmed specimens stretched in the perpendicular direction, indicating that the strain variation and the axial strain patterns were caused by local mesogen relaxation. Mesogen relaxation was apparent in the polydomain for strain rates of $0.1/s$ and lower. In contrast, mesogen relaxation in the 90% perpendicular specimen occurred over a broader range of strain rates and was apparent even at the largest 10%/s strain rate.
- The Poisson's ratio, measured from the DIC lateral strain response, was insensitive to strain rate. The 90% perpendicular specimen exhibited a Poisson's ratio of 1, indicating that deformation occurred mainly from mesogen rotation. All other specimens, including the polydomain and 30% perpendicular specimens that exhibited a soft stress response, exhibited a Poisson's ratio of 0.5, indicating typical network deformation mechanism.

Altogether, the findings suggests that the rate-dependence of the stress response for the polydomain and 30% pre-stretched network arose mainly from the relaxation dynamics of the networks chains. Mesogen relaxation contributed

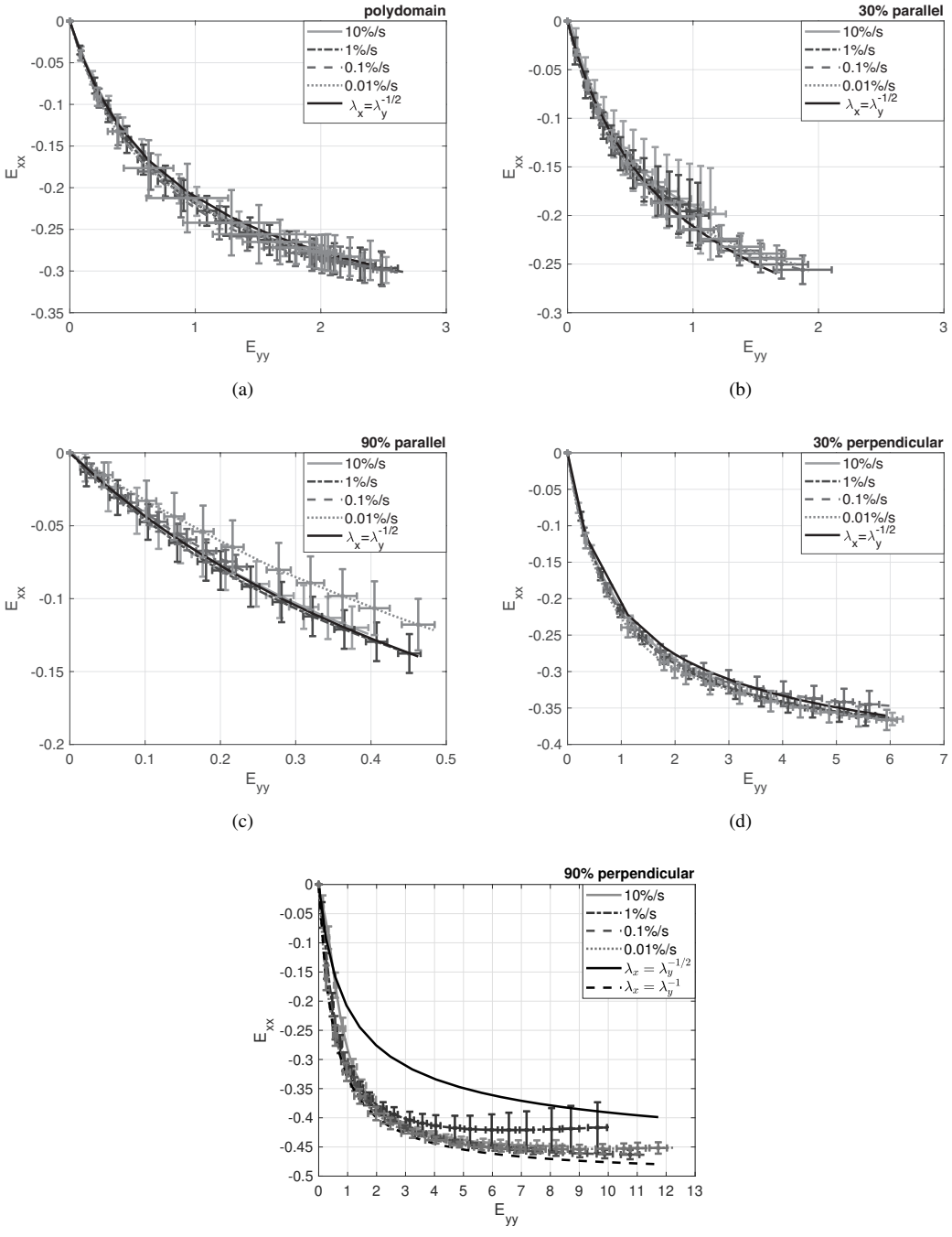

Figure 10: The specimen-averaged Green-Lagrange lateral strain E_{xx} vs. axial strain E_{yy} for representative tests for different LCE networks and loading directions: (a) 0% polydomain, (b) 30% parallel, (c) 90% parallel, (d) 30% perpendicular, and (e) 90% perpendicular. The error bars show the standard deviation in E_{xx} (vertical bar) and E_{yy} (horizontal bar). Also plotted for all specimens is the prediction of the semi-soft elasticity theory for the lateral contraction of an isotropic network, $\lambda_x = \lambda_y^{-1/2}$. The theoretical prediction for the lateral contraction, $\lambda_x = \lambda_y^{-1}$, in the soft stress region where mesogen rotation dominates is also plotted for the 90% perpendicular specimen. The E_{xx} measured for the 90% perpendicular specimen agreed well with the theoretical prediction for mesogen rotation, while the E_{xx} measured for all other specimens followed the prediction for network deformation.

mainly to the softening of the stress response. This may explain why Azoug *et al.* [9] was able to apply the temperature shift factors measured at small strains to construct master curves for the peak stress and the beginning and end strain of the soft stress response. The lateral contraction measurements showed that the soft stress response of the 90% perpendicular specimen occurred primarily through mesogen rotation. The 90% perpendicular specimen also had a weaker rate-dependence for the hysteresis and Young's modulus and a larger temperature range $T_g^{onset} - T_{ni}$ in the DMA tests. The latter suggests that alignment produced a broader relaxation spectrum that exteded faster relaxation times. This may explain why mesogen relaxation in the 90% perpendicular occurred over a broader range of strain rates and at higher strain rates than in the polydomain specimen.

There are several important limitations of this work. Primarily, the experiments explored a narrow range of strain rates, from 0.01%/s -10%/s. Slower rates can be achieved in a quasi-equilibrium test where the deformation is applied in steps with long equilibrium times between each step [14] or through higher temperatures using time-temperature superposition [9]. We did not test the specimens at the same temperature above their respectively T_g^{onset} because the temperature chamber did not have a transparent window for DIC. The second stage pre-stretching method of monodomain formation aligned both the networks chains and mesogen domains. In future work, we plan to investigate the separate effects of chain and mesogen alignment by using a bond-exchange reaction to relax the chain alignment after the second-stage crosslinking [39]. While the DIC strain measurements showed the development of a heterogeneous strain field, it did not have sufficient resolution to identify the presence of stripe domains and other microtructural features. The DIC measurement motivate the need for microstructural characterization studies and computational modeling studies to determine the nonunifomr domain/mesogen structure underlying the strain patterns.

Despite the limitations, this study further revealed the effects of alignment on the rate-dependence and mechanical damping of LCEs, provided characterizations of the rate-dependence of mesogen relaxation, and further insights on the mechanisms underlying the rate-dependence and dissipation behavior of main-chain LCEs. The broader impacts of this study further advance the understanding of the mechanical responses of LCEs towards being able to create tailored materials and structures with novel mechanical behaviors. The alignment of these materials during synthesis can be used to impart a designed anisotropic response. For example, the soft stress behavior of a monodomain LCE can be eliminated or enhanced if aligned parallel or perpendicular to the direction of tensile loading to impart an anisotropic energy absorption capability. Desired features for mechanical energy dissipation, such as strain-to-failure, the soft-stress response, hysteresis, and peak stress, are enhanced in the material if monodomain LCEs are strained perpendicular to the director. This would be especially beneficial when trying to mimic biological tissues, such as the annulus fibrosis of an intervertebral disc, which has a stiff elastic response in one direction and soft-dampening in the other, in the design of medical devices. Researchers have already demonstrated direct ink writing (DIW) printing techniques to create LCEs with complex alignment patterns. As a result, it is possible that these techniques will pave the way to design devices and structures with spatially and directionally tuned modulus, energy absorption, and wave propagation properties. Recent studies have demonstrated direct ink writing printing techniques to create LCEs with complex alignment patterns [40, 41]. area. As a result, it is possible that these techniques will pave the way to design devices and structures with spatially and directionally tuned modulus, energy absorption, and wave propagation properties.

Acknowledgments

The authors gratefully acknowledge the funding support from the US Army Research Office (W911NF-17-1-0165).

References

[1] M. Warner and XJ J. Wang. Elasticity and phase behavior of nematic elastomers. *Macromolecules*, 24(17):4932–4941, aug 1991.

[2] Kathrin Hammerschmidt and Heino Finkelmann. Stress-optical and thermomechanical measurements on liquid crystalline elastomers. *Makromol. Chemie*, 190:1089–1101, 1989.

[3] Jürgen Küpfer and Heino Finkelmann. Nematic liquid single crystal elastomers. *Makromol. Chemie, Rapid Commun.*, 12:717–726, 1991.

[4] Jürgen Küupfer and Heino Finkelmann. Liquid crystal elastomers: Influence of the orientational distribution of the crosslinks on the phase behaviour and reorientation processes. *Macromol. Chem. Phys.*, 195(4):1353–1367, apr 1994.

[5] S. M Clarke, A. Hotta, a. R Tajbakhsh, and E. M Terentjev. Effect of crosslinker geometry on equilibrium thermal and mechanical properties of nematic elastomers. *Phys. Rev. E*, 64(6):061702, nov 2001.

[6] S. M. Clarke, E. M. Terentjev, I. Kundler, and H. Finkelmann. Texture Evolution during the Polydomain-Monodomain Transition in Nematic Elastomers. *Macromolecules*, 31(15):4862–4872, jul 1998.

[7] A Hotta and E M Terentjev. Dynamic soft elasticity in monodomain nematic elastomers. *Eur. Phys. J. E*, 10(4):291–301, 2003.

[8] S. M. Clarke, a. R. Tajbakhsh, E. M. Terentjev, C. Remillat, G. R. Tomlinson, and J. R. House. Soft elasticity and mechanical damping in liquid crystalline elastomers. *J. Appl. Phys.*, 89(11):6530, 2001.

[9] A. Azoug, V. Vasconcellos, J. Dooling, M. Saed, C.M. M. Yakacki, and T.D. D. Nguyen. Viscoelasticity of the polydomain-monodomain transition in main-chain liquid crystal elastomers. *Polymer (Guildf).*, 98:165–171, aug 2016.

[10] Daniel R. Merkel, Rajib K. Shaha, Christopher M. Yakacki, and Carl P. Frick. Mechanical energy dissipation in polydomain nematic liquid crystal elastomers in response to oscillating loading. *Polymer (Guildf).*, 166:148–154, mar 2019.

[11] Christian Ohm, Martin Brehmer, and Rudolf Zentel. Liquid Crystalline Elastomers as Actuators and Sensors. *Adv. Mater.*, 22(31):3366–3387, may 2010.

[12] S. V. Fridrikh and E. M. Terentjev. Polydomain-monodomain transition in nematic elastomers. *Phys. Rev. E*, 60(2):1847–1857, aug 1999.

[13] Jonathan K Whitmer, Tyler F Roberts, Raj Shekhar, Nicholas L Abbott, and Juan J. De Pablo. Modeling the polydomain-monodomain transition of liquid crystal elastomers. *Phys. Rev. E - Stat. Nonlinear, Soft Matter Phys.*, 87(2):1–5, 2013.

[14] S. M Clarke and E. M Terentjev. Slow stress relaxation in liquid crystal elastomers and gels. *Faraday Discuss.*, 112(20):325–333, nov 1999.

[15] A Hotta and E. M. Terentjev. Long-time stress relaxation in polyacrylate nematic liquid crystalline elastomers. *J. Phys. Condens. Matter*, 13:11453–11464, 2001.

[16] Kenji Urayama, Etsuko Kohmon, Masahiro Kojima, and Toshikazu Takigawa. Polydomain-Monodomain Transition of Randomly Disordered Nematic Elastomers with Different Cross-Linking Histories. *Macromolecules*, 42(12):4084–4089, jun 2009.

[17] C Ortiz, C. K. Ober, and E J Kramer. Stress relaxation of a main-chain, smectic, polydomain liquid crystalline elastomer. *Polymer (Guildf).*, 39(16):3713–3718, 1998.

[18] Kenji Urayama, Seiji Honda, and Toshikazu Takigawa. Slow dynamics of shape recovery of disordered nematic elastomers. *Phys. Rev. E*, 74(4):041709, oct 2006.

[19] Kenji Urayama, Hidesato Kondo, Yuko O. Arai, and Toshikazu Takigawa. Electrically driven deformations of nematic gels. *Phys. Rev. E*, 71(5):051713, may 2005.

[20] P Stein, N Aßfalg, H Finkelmann, and P Martinoty. Shear modulus of polydomain, mono-domain and non-mesomorphic side-chain elastomers: Influence of the nematic order. *Eur. Phys. J. E*, 4(3):255–262, mar 2001.

[21] Daniel R. Merkel, Nicholas A. Traugutt, Rayshan Visvanathan, Christopher M. Yakacki, and Carl P. Frick. Thermomechanical properties of monodomain nematic main-chain liquid crystal elastomers. *Soft Matter*, 14(29):6024–6036, 2018.

[22] S. M. Clarke, A. Hotta, A. R. Tajbakhsh, and E. M. Terentjev. Effect of cross-linker geometry on dynamic mechanical properties of nematic elastomers. *Phys. Rev. E*, 65(2):021804, jan 2002.

[23] S. M. Clarke, A. R. Tajbakhsh, E. M. Terentjev, and M. Warner. Anomalous Viscoelastic Response of Nematic Elastomers. *Phys. Rev. Lett.*, 86(18):4044–4047, apr 2001.

[24] Robyn H. Pritchard, Pascal Lava, Dimitri Debruyne, and Eugene M. Terentjev. Precise determination of the Poisson ratio in soft materials with 2D digital image correlation. *Soft Matter*, 2013.

[25] T. H. Ware and T. J. White. Programmed liquid crystal elastomers with tunable actuation strain. *Polym. Chem.*, 6(26):4835–4844, 2015.

[26] C. M. Yakacki, M. Saed, D. P. Nair, T. Gong, S. M. Reed, and C. N. Bowman. Tailorable and programmable liquid-crystalline elastomers using a two-stage thiolacrylate reaction. *RSC Adv.*, 5(25):18997–19001, 2015.

[27] Mohand O. Saed, Amir H. Torbati, Chelsea A. Starr, Rayshan Visvanathan, Noel A. Clark, and Christopher M. Yakacki. Thiol-acrylate main-chain liquid-crystalline elastomers with tunable thermomechanical properties and actuation strain. *J. Polym. Sci. Part B Polym. Phys.*, 55(2):157–168, jan 2017.

[28] Mohand O. Saed, Amir H. Torbati, Devatha P. Nair, and Christopher M. Yakacki. Synthesis of Programmable Main-chain Liquid-crystalline Elastomers Using a Two-stage Thiol-acrylate Reaction. *J. Vis. Exp.*, 107, jan 2016.

[29] O. Kratky. Zum Deformationsmechanismus der Faserstoffe, I. *Kolloid-Zeitschrift*, 64(2):213–222, aug 1933.

[30] Mark T. Sims, Laurence C. Abbott, Robert M. Richardson, John W. Goodby, and John N. Moore. Considerations in the determination of orientational order parameters from X-ray scattering experiments. *Liq. Cryst.*, 46(1):11–24, jan 2019.

[31] Gerd H. F. Bergmann, Heino Finkelmann, Virgil Percec, and Mingyang Zhao. Liquid-crystalline main-chain elastomers. *Macromol. Rapid Commun.*, 18(5):353–360, may 1997.

[32] P. Martinoty, P. Stein, H. Finkelmann, H. Pleiner, and H. R. Brand. Mechanical properties of mono-domain side chain nematic elastomers. *Eur. Phys. J. E*, 14(4):311–321, aug 2004.

[33] Eugene R. Zubarev, Sergei A. Kuptsov, Tatyana I. Yuranova, Raissa V. Talrose, Heino Finkelmann, R. V. Talroze, and Heino Finkelmann. Monodomain liquid crystalline networks: reorientation mechanism from uniform to stripe domains. *Liq. Cryst.*, 26(10):1531–1540, oct 1999.

[34] Haruko Higaki, Toshikazu Takigawa, and Kenji Urayama. Nonuniform and Uniform Deformations of Stretched Nematic Elastomers. *Macromolecules*, 46(13):5223–5231, jul 2013.

[35] S Conti. Soft elastic response of stretched sheets of nematic elastomers: a numerical study. *J. Mech. Phys. Solids*, 50(7):1431–1451, jul 2002.

[36] M. Schönstein, W. Stille, and G. Strobl. Effect of the network on the director fluctuations in a nematic side-group elastomer analysed by static and dynamic light scattering. *Eur. Phys. J. E*, 5(5):511–517, aug 2001.

[37] G. C. Verwey and M. Warner. Compositional Fluctuations and Semisoftness in Nematic Elastomers. *Macromolecules*, 30(14):4189–4195, jul 1997.

[38] Mark Warner and Eugene Terentjev. *Liquid Crystal Elastomers*. Oxford University Press, 2003.

[39] Drew W. Hanzon, Nicholas A. Traugutt, Matthew K. McBride, Christopher N. Bowman, Christopher M. Yakacki, and Kai Yu. Adaptable liquid crystal elastomers with transesterification-based bond exchange reactions. *Soft Matter*, 14(6):951–960, 2018.

[40] Arda Kotikian, Ryan L. Truby, John William Boley, Timothy J. White, and Jennifer A. Lewis. 3D Printing of Liquid Crystal Elastomeric Actuators with Spatially Programed Nematic Order. *Adv. Mater.*, 30(10):1706164, mar 2018.

[41] Sabina W. Ula, Nicholas A. Traugutt, Ross H. Volpe, Ravi R. Patel, Kai Yu, and Christopher M. Yakacki. Liquid crystal elastomers: an introduction and review of emerging technologies. *Liq. Cryst. Rev.*, 6(1):78–107, jan 2018.

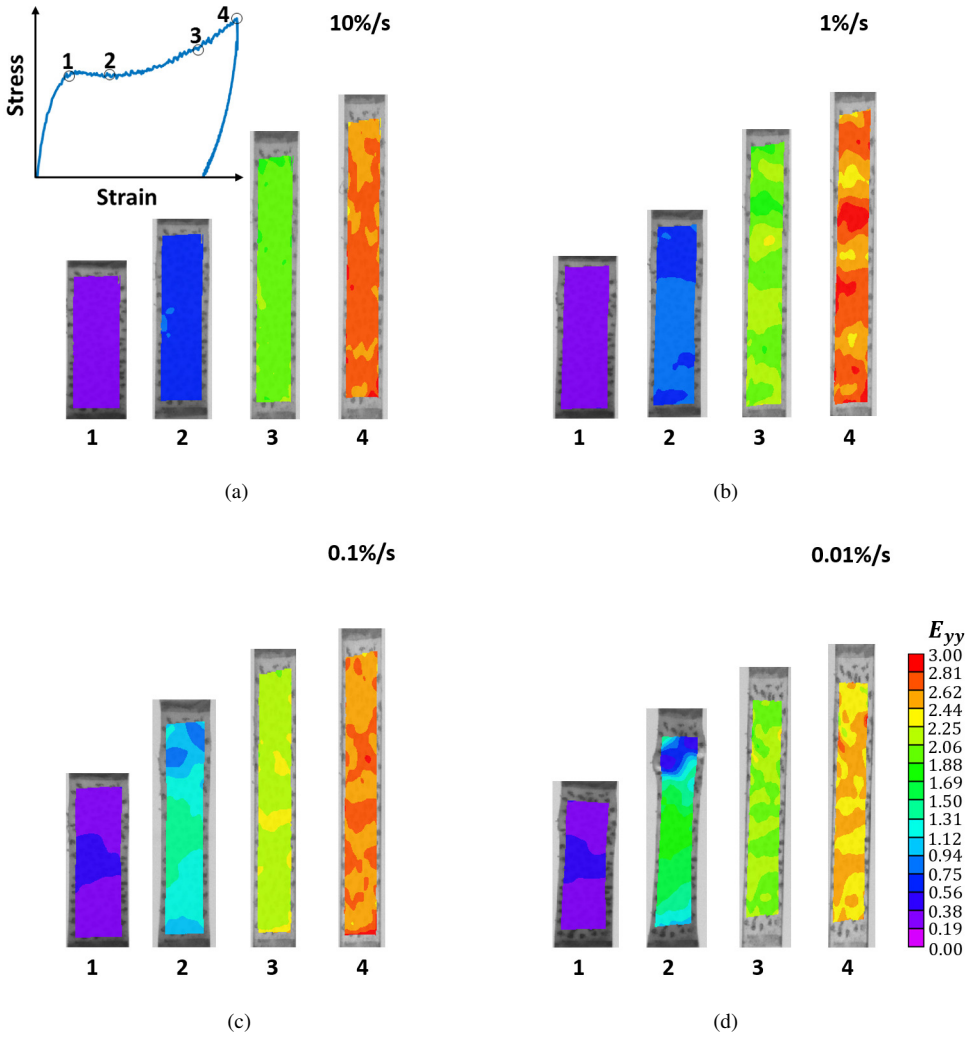

Figure 1: Strain contours for the Green-Lagrange axial strain E_{yy} measured using 3D DIC at 4 points in the soft-stress response for representative tests of polydomain specimens at (a) 10%/s, (b) 1%/s, (c) 0.1%/s, and (d) 0.01% strain rates. The contours are plotted over the deformed specimen. An example of the stress-strain curve is also included to indicate the four points in the soft stress response: 1- the starting point for softening; 2- strain softening; 3-strain hardening; and 4- the maximum stretch.

The effect of alignment on the rate-dependent behavior of a main-chain liquid crystal elastomers

Cristina P. Martin Linares[a], Nicholas A. Traugutt[b], Mohand Saed[c], Alejandro Martin Linares[a], Christopher M. Yakacki[b], Thao D. Nguyen[a,*]

[a]*Department of Mechanical Engineering, The Johns Hopkins University, Baltimore, MD, USA*
[b]*Department of Mechanical Engineering, University of Colorado Denver, Denver, CO, USA*
[c]*Department of Physics, University of Cambridge, Cambridge, UK*

Abstract

This study investigated the effect of alignment on the rate-dependent behavior of a main-chain liquid crystal elastomer (LCE). Polydomain nematic LCE networks were synthesized from a thiol-acrylate Michael addition reaction in the isotropic state. The polydomain networks were stretched to different strain levels to induce alignment then crosslinked in a second stage photopolymerization process. The LCE networks were subjected to dynamic mechanical tests to measure the temperature-dependent storage modulus and uniaxial tension load-unload tests to measure the rate-dependence of the Young's modulus, mechanical dissipation, and characteristics of the soft stress response. Three-dimensional (3D) digital image correlation (DIC) was used to characterize the effect of domain/mesogen relaxation on the strain fields. All LCE networks exhibited a highly rate-dependent stress response with significant inelastic strains after unloading. The Young's modulus of the loading curve and hysteresis of the load-unload curves showed a power-law dependence on the strain rate. The Young's modulus increased with alignment and larger anisotropy and a smaller power-law exponent was measured for the Young's modulus and hysteresis for the highly aligned monodomains. The polydomain and pre-stretched networks loaded perpendicular to the alignment direction exhibited a soft stress response that featured a rate-dependent peak stress, strain-softening, and strain-stiffening. The 3D-DIC strain fields for the polydomain network and programmed networks stretched in the perpendicular direction were highly heterogeneous, showing regions of alternating higher and lower strains. The strain variations increased initially with loading, peaked during the strain softening part of the stress response, then decreased during the strain stiffening part of the stress response. Greater variability was measured for lower strain rates. These observations suggest that local domain/mesogen relaxation led to the development of the heterogeneous strain patterns and strain softening in stress response. Figure 1 shows the strain contour patterns as a function of strain rate for polydomain. These findings improved understanding of the kinetics of mesogen relaxation and its contributions to the rate-dependent stress response and mechanical dissipation.

*Corresponding author
Email address: vicky.nguyen@jhu.edu (Thao D. Nguyen)